

# **Nanoscale MnO<sub>2</sub> cathodes for Li-ion batteries; Effect of thermal and mechanical processing**

<sup>1</sup>Elahe Moazzen, <sup>2</sup>Kamil Kucuk, <sup>3</sup>Shankar Aryal, <sup>1</sup>Elena V. Timofeeva, <sup>2</sup>Carlo U. Segre

<sup>1</sup>Department of Chemistry, Illinois Institute of Technology, 3101 S. Dearborn Street, Chicago, Illinois 60616, United States

<sup>2</sup>Department of Physics & CSRRI, Illinois Institute of Technology, 3101 S. Dearborn Street, Chicago, Illinois 60616, United States

<sup>3</sup>Applied Materials Division, Argonne National Laboratory, Lemont, Illinois 60439, United States

## **Abstract**

This study investigates the effect of thermal and mechanical processing of MnO<sub>2</sub> nanoparticle cathodes on the electrochemical performance, ion intercalation mechanism and structural changes upon cycling. Thermal processing at different temperatures is utilized to tune the sub-nanoparticle polymorph composition, while mechanical processing (high energy ball-milling) is used to change the particle size and create a better contact between active material and conductive graphite additive. The combination of thermal and mechanical processing is also investigated for possible synergistic effects. The structural changes due to processing suggest that thermal treatment of the MnO<sub>2</sub> nanoparticles at 400 °C forms a high concentration of pyrolusite domains (1 × 1 channels) leading to improved reversibility of lithium intercalation/de-intercalation and capacity retention. It is also found that ball-milling for a short time (20 min) leads to some amorphization and decrease of the crystallite sizes resulting in

higher concentration of  $1 \times 1$  channels and improved capacity. The structural changes and ion intercalation mechanism of the pristine and processed electrode materials during cycling are investigated by *ex situ* synchrotron x-ray diffraction (XRD) and *ex situ* and *in situ* x-ray absorption near edge structure (XANES) studies.

## Key words

Lithium-ion battery, cathode, manganese dioxide, synchrotron x-ray diffraction, synchrotron x-ray absorption spectroscopy, lithium manganese oxide, phase composition, ball-milling, thermal treatment, nanoparticles.

## Introduction

Among Li-ion battery (LIB) cathodes, manganese dioxide compounds have attracted significant attention due to their low cost, nontoxic nature and high theoretical capacity of  $308 \text{ mAh g}^{-1}$  for one electron transfer [1].  $\text{MnO}_2$  is the most common cathode material in primary Li-ion batteries, and has also been investigated for use in secondary Li-ion batteries [2]. However, this material suffers from rapid capacity fading in LIB electrolytes. The  $\text{MnO}_2$  polymorphs most commonly considered as battery cathodes are ramsdellite (R- $\text{MnO}_2$ ,  $1 \times 2$  channels), pyrolusite ( $\beta$ - $\text{MnO}_2$ ,  $1 \times 1$  channels), akhtenskite ( $\epsilon$ - $\text{MnO}_2$ ), gamma ( $\gamma$ - $\text{MnO}_2$ ), and electrolytic manganese oxide (EMD- $\text{MnO}_2$ ) that have a mixture of  $1 \times 2$  and  $1 \times 1$  channels and defects [3-11]. The challenges associated with using EMD as the most common cathode in LIB electrolyte include presence of water, specifically  $\text{OH}^-$  ions, within the  $\text{MnO}_2$  crystal lattice, which decreases the material's density and specific capacity and causes gassing during cycling in LIB electrolytes[2,9,12,13,14]. Therefore, thermal treatment of EMD- $\text{MnO}_2$  at temperatures above  $300 \text{ }^\circ\text{C}$  has been proposed as a necessary step before cycling to remove structural water [15].

Other important factors often overlooked in studies of manganese oxide cathodes are the polymorph composition and structural properties, which vary significantly with synthesis and heat treatment conditions [16-18]. Previously, we have reported on the significance of MnO<sub>2</sub> polymorph composition in the redox mechanisms in aqueous electrolytes. Thermal treatment results in gradual change of polymorph composition through the conversion of 1 × 2 channels to 1 × 1 channels [18]. The lack of such characterization for the EMD starting material and annealed products is likely the cause of significant inconsistencies in the electrochemical results for HEMD as LIB cathodes [12, 13, 19-21]. To the best of our knowledge, systematic investigation of thermal and mechanical processing on performance of MnO<sub>2</sub> nanoparticles as LIB cathodes has not been done before and is presented in this paper.

An *in situ* XRD study of HEMD treated at 350 °C under air showed variation in first discharge capacities (105 to 256 mAh g<sup>-1</sup>) for samples with different polymorph composition, crystallite size, and surface area and showed that a higher fraction of pyrolusite in the treated sample favors higher initial capacity and faster discharge rates in LIB electrolytes [19]. HEMD treated at 400 °C under N<sub>2</sub> showed high capacity for the first discharge (270 mAh g<sup>-1</sup>) followed by capacity loss when cycled between 2-3.8 V. The structural changes in the electrode material during cycling were investigated with *ex situ* XRD and it was found that on the initial stages of discharge, pyrolusite tetragonal unit cells start to expand due to Li-ion insertion followed by conversion to an orthorhombic crystalline structure (Li<sub>x</sub>MnO<sub>2</sub>), which is rechargeable in Li-ion electrolyte shrinking and expanding anisotropically (within 10% in unit cell volume) [13]. Tan et al. reported ~225 mAh g<sup>-1</sup> first discharge capacity for HEMD treated at 375 °C in air (β/γ-MnO<sub>2</sub>, mainly β-MnO<sub>2</sub>) which degraded to ~130 mAh g<sup>-1</sup> in the second cycle and reached 70 mAh g<sup>-1</sup> after 100 cycles [14].

Loss of electrical connectivity between nanoparticles and the current collector is often reported as a cause for rapid capacity degradation. Ball-milling of active electrode materials with conductive additive has been reported to improve the capacity and cycle life of Li-ion battery electrodes due to crystal size reduction and better electrical contact of nanoparticles with the current collector [22-25]. Ball-milling of alpha MnO<sub>2</sub> with carbon nanotubes (6 : 4 weight ratio)

improved the initial specific capacitance ( $160 \text{ F g}^{-1}$  vs  $127 \text{ F g}^{-1}$ ) of the composite [26]. Improvement to both specific capacity and cycle performance was demonstrated for ball-milled  $\text{Sn}_4\text{P}_3$ /graphite composite [25] due to amorphization of active material which helped reversibility of the redox reaction. In this study we systematically investigate the effect of ball-milling of  $\text{MnO}_2$  nanoparticles with graphite on the cycling performance as LIB cathodes and redox mechanisms through detailed characterization of structural changes within the material. Additionally the effect of combining of thermal and mechanical processing on the active material is also reported.

This work provides fundamental understanding of the mechanisms behind the benefits of thermal and mechanical processing for cathode materials using *ex situ* synchrotron XRD, *ex situ* and *in situ* synchrotron XAS and will be insightful for researchers working on improving performance of LIB electrodes.

## Experimental

### $\text{MnO}_2$ nanoparticles synthesis

$\text{MnO}_2$  nanoplatelets were synthesized by dissolving 4.00 g of  $\text{MnSO}_4 \cdot \text{H}_2\text{O}$  (Acros Organics) in 430 mL DI water followed by addition of 45.07 g of the oxidizing agent  $\text{Na}_2\text{S}_2\text{O}_8$  (Sigma-Aldrich). The clear solution was heated to  $100^\circ\text{C}$  under magnetic stirring and held at that temperature for 450 min. The nanoparticles were filtered, washed with DI water and dried at  $90^\circ\text{C}$ . The average yield of the reaction was  $90 \pm 2\%$ . All nanoparticles used in this study were from the same batch.

### Thermal treatment of $\text{MnO}_2$ nanoparticles

Per thermogravimetric analysis (TGA) of the pristine sample (Figure S1, supplemental information), the nanopowder was heat-treated at temperatures,  $270^\circ\text{C}$ ,  $320^\circ\text{C}$  and  $400^\circ\text{C}$ , representative of different hydration states, for 5 h in a tube furnace under static air atmosphere

[18]. The as-synthesized (pristine) and annealed samples are abbreviated as P, A270, A320 and A400 throughout the manuscript.

### **Ball-milling of MnO<sub>2</sub> nanoparticles with graphite nanoplatelets**

In this series of samples, graphite nanoplatelets (GNP-M5, XGSciences) were used as a conductive carbon additive. 1.30 g of MnO<sub>2</sub> nanoparticles, 0.37 g of graphite nanoplatelets (70 : 20 wt% ratio) and 30 of 0.25” stainless steel balls (McMaster-Carr) were placed in a stainless steel vessel and processed in a high energy ball-mill (MTI MSK-SFM-3, 1400 rpm) for 20 min, 40 min and 60 min. Resulting samples are labeled as B20, B40 and B60, respectively throughout the manuscript.

### **Li-ion cell preparation**

The MnO<sub>2</sub> electrodes for Li-ion coin cells and in situ pouch cells were prepared by casting slurries composed of 70 : 20 : 10 weight ratio of active material, acetylene carbon black conductive filler (STREM Chemicals) and polyvinylidene fluoride (PVDF, Sigma Aldrich) binder in 1-methyl-2-pyrrolidinone (NMP, Sigma Aldrich) solvent on an aluminum current collector (0.018 mm thick) using a doctor blade. For the nanopowders ball-milled with GNP, the slurry was composed of 90 : 10 weight ratio of ball-milled sample (containing 70 : 20 wt% ratio of MnO<sub>2</sub> : graphite) and PVDF. The coin cells (CR2032) were assembled inside an argon-filled glovebox using an automated cell crimper (MSK-160D1, MTI Corporation) with Li foil as anode (0.2 mm thick, Goodfellow), a porous membrane separator (Celgard 2325) and 1.2M LiPF<sub>6</sub> in 3 : 7 volume ratio of ethylene carbonate, ethyl methyl carbonate as electrolyte (Tomiya Chemicals).

## Electrochemical characterization

Cyclic voltammetry of the coin cells was conducted between 1.7 V and 4.5 V at 0.5 mVs<sup>-1</sup> using a EzStat Pro potentiostat/galvanostat (Nuvant Systems, Inc); galvanostatic cycling in the potential range between 1.8 V and 4.5 V was performed using a battery cycler (BST8-MA, MTI Corporation) at C/10 charge rate. The cycling results presented are the average values of at least two cells.

## X-ray powder diffraction

The crystallographic structure of the nanoparticles was identified by X-ray powder diffraction (XRD, Bruker D2 Phaser with a LynxEye detector and Cu-K $\alpha$  source with  $\lambda = 1.54 \text{ \AA}$ ). The diffraction patterns were measured over a  $2\theta$  range of 10–100 with 0.02  $2\theta$  step and 8 s/step dwell time. The high resolution synchrotron XRD ( $\lambda = 0.41 \text{ \AA}$ ) measurements were conducted at the 11-BM beamline of the Advanced Photon Source at Argonne National Laboratory. The diffraction patterns were collected with 0.001°  $2\theta$  step size and 0.1 s/step dwell time. The synchrotron x-ray diffraction patterns ( $\lambda = 0.41 \text{ \AA}$ ) were converted to Cu-K $\alpha$  radiation ( $\lambda = 1.54 \text{ \AA}$ ) using Bragg's Law for comparison purposes.

The ex situ samples were prepared from cycled electrodes, extracted from coin cells. The electrodes were separated from the aluminum foil current collectors and sealed for the measurement using adhesive Kapton tape. Samples were stored under Ar atmosphere until the measurement.

To obtain information on particle size, phase composition and ratio of the phases in each sample, XRD patterns were refined by the Rietveld method using GSAS and EXPGUI software packages [27-29]. ICSD crystallographic information [30] was used as a starting point for all refinements.

## **X-ray absorption spectroscopy**

To investigate the oxidation state changes occurring during processing and cycling of the electrodes *ex situ* and *in situ* x-ray absorption spectroscopy (XAS) measurements were performed at the Materials Research Collaborative Access Team (MRCAT), 10-BM and 10-ID beamlines [31, 32], at the Advanced Photon Source. The Si(111) double crystal monochromator was calibrated by using a standard Mn foil to measure Mn K-edge (6537.75 eV) XAS. Gas filled ion chambers were utilized to measure the x-ray intensities:  $I_0$  (before x-ray and sample interaction),  $I_t$  (after transmitting through the sample), and  $I_r$  (fluorescence x-rays emitted after interaction). The XAS spectra were aligned, merged and normalized using the Athena software from the IFEFFIT package [33, 34]. The *in situ* custom pouch cells were assembled using lithium foil as the counter electrode, porous membrane separator and the electrolyte, inside an argon-filled glovebox. The cells were vacuum sealed inside the glovebox and covered with adhesive Kapton tape. The pouch cells were cycled in the beamline using a EZ-potentiostat, while *in situ* XAS spectra were collected as continuous scans in fluorescence mode using a Lytle detector fluorescence ion chamber.

## **Scanning electron microscopy**

Size and morphology of nanoparticles were examined by scanning electron microscopy (SEM, Hitachi S-4700) and statistically analyzed using ImageJ software [35]. Samples for SEM were prepared by drop-casting dilute suspensions of nanoparticles in ethanol onto a silicon wafer.

## **Results and discussion**

### **Thermal treatment of MnO<sub>2</sub> nanoparticles**

The average size of pristine MnO<sub>2</sub> nanoplatelets (P) was estimated to be 140±22 nm in diameter and 24±6 nm in thickness by analysis of SEM images (Figure S1, supplemental information).

Annealed nanopowders showed no significant difference in morphology, consistent with previously reported results [18].

Rietveld refinement (Table 1) of the pristine MnO<sub>2</sub> nanoparticles showed a polymorph composition of 37±1 wt% ramsdellite and 63±1 wt% akhtenskite and an average grain size of 3 × 3 nm for ramsdellite and 17 × 10 nm for akhtenskite (Figure S2, supplemental information). Thermal treatment at 270 °C and 320 °C resulted in partial conversion of both phases to gamma phase due to structural water removal, while treatment at 400 °C results in complete conversion to pyrolusite due to conversion of 1 × 2 channels to 1 × 1 channels [18]. Changes in crystalline sizes (Table 1) also show dynamic conversion of phases with thinning of ramsdellite and growth of gamma domains as the treatment temperature increases.

XANES analysis (Figure S3, supplemental information) of the pristine nanoparticles showed the presence of mixed valence Mn<sup>3+</sup>/Mn<sup>4+</sup> sites, which are likely coordinated with H<sup>+</sup> ions due to the aqueous synthesis of pristine MnO<sub>2</sub> nanopowder. In thermally treated samples the edge positions were shifted toward higher energies, indicating an increase in average oxidation state with increase in annealing temperature, which is consistent with water removal by thermal treatment (Figure 1a).

Table 1. Rietveld refinement results of the XRD patterns of the pristine and heat treated samples.

	Ramsdellite		Akhtenskite		Gamma		Pyrolusite	
	wt%	crystallite size (nm)	w%	crystallite size (nm)	wt%	crystallite size (nm)	wt%	crystallite size (nm)
P	37 ± 1	3 × 3	63 ± 1	17 × 10	-	-	-	-
A270	28 ± 1	6 × 1	51 ± 1	16 × 7	21 ± 1	15 × 3	-	-
A320	21 ± 1	2 × 19	51 ± 1	18 × 5	28 ± 1	28 × 28	-	-
A400	-	-	37 ± 1	14 × 11	-	-	63 ± 1	2 × 7

The first CV cycles of the pristine and annealed MnO<sub>2</sub> nanoparticles (Figure 1b) show multiple oxidation peaks in the range between 2.8 V and 4.5 V, related to variation in phase composition and differing electrochemical activity of MnO<sub>2</sub> polymorphs. The shift in potentials between the cathodic and anodic peaks decreases as the temperature of the treatment increases, suggesting better redox reversibility.

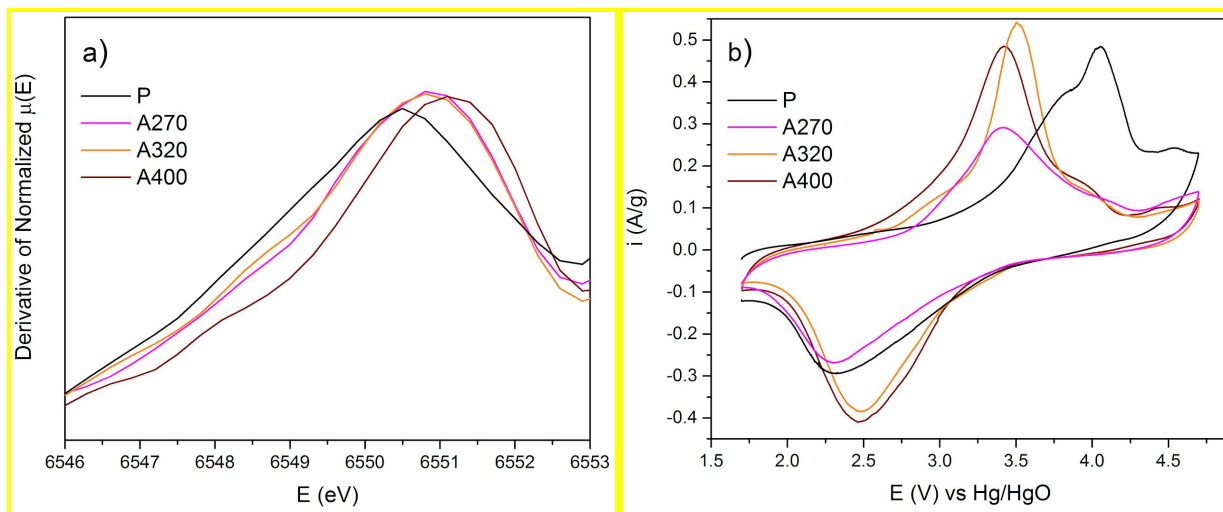


Figure 1. a) The derivatives of the XANES regions for pristine and annealed MnO<sub>2</sub> nanoparticles from the *ex situ* XAS spectra at Mn K-edge and b) cyclic voltammograms of the pristine and annealed samples at 1<sup>st</sup> cycle and at 0.5 mVs<sup>-1</sup>.

Galvanostatic cycling of the electrodes (Figure 2a) showed the highest first discharge capacity in pristine and A400 samples, 278 mAh g<sup>-1</sup> and 283 mAh g<sup>-1</sup>, respectively, but differing capacity fading behavior is observed across the series (Table 2). After an initial capacity drop (25 cycles) the annealed samples show much slower capacity degradation than the pristine material. The A400 sample with the highest fraction of pyrolusite showed the best capacity retention of 77% after 100 cycles, consistent with better peak reversibility of pyrolusite MnO<sub>2</sub> polymorph with 1 × 1 channels observed in CV measurements.

Two-step reduction has been reported for HEMD in LIB electrolyte. During initial discharge pyrolusite domains first irreversibly convert to a lithiated phase ( $\text{Li}_x\text{MnO}_2$ ) followed by the reversible lithiation of this new phase through insertion of additional lithium [2, 13, 16]. The fraction of lithiated phase gradually displaces the original HEMD [2]. A similar mechanism was proposed for ramsdellite  $\text{MnO}_2$  - formation of orthorhombic  $\text{Li}_x\text{MnO}_2$  in the initial stages of lithiation ( $0 \leq x \leq 0.3$ ) of the hexagonal-close-packed structure of ramsdellite, followed by the complete conversion to  $\text{LiMnO}_2$  in deep discharge [17].

As per XANES results, the pristine material (P) showed some fraction of  $\text{Mn}^{3+}$  (Figure S3, supplemental information), the galvanostatic cycling of the cells always started with charge to bring the cathode material to more uniform  $\text{Mn}^{4+}$  lattice for Li intercalation (Figure S4, supplemental information). From the capacity of the first charge it can be estimated that ~56% of Mn sites are oxidized on the first charge, which is consistent with a shift to higher energies of the XANES. Lithiation of  $\text{MnO}_2$  in the first discharge (Figure 2b), shows a broad plateau at ~2.7 V corresponding to the intercalation of Li-ions into ramsdellite and aktenskite phases of the original material. The second charge capacity is very close to that of the first discharge with a distinct plateau at 3.1 V (Figure 2b). In the second discharge two distinct plateaus are observed at 2.8 V and 3.2 V, which are different from the broad plateau on the first discharge, clearly indicating the formation of a new phase. These features remain in the 100<sup>th</sup> charge and discharge curves with significantly lower capacity (Figure 2b), which shows loss of redox activity of the newly formed phase.

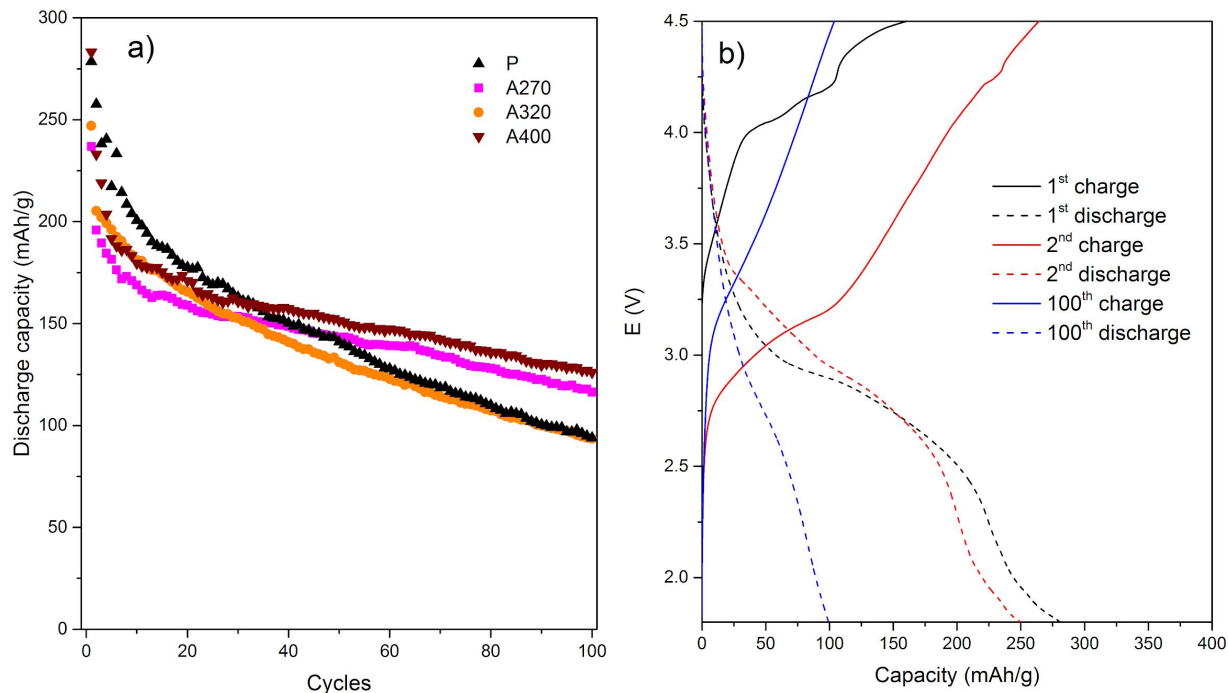


Figure 2. a) Galvanostatic cycling of the pristine at C/10 charge rate and heat-treated MnO<sub>2</sub> nanoparticles and b) Galvanostatic charge/discharge curves for the pristine MnO<sub>2</sub> nanoparticles.

*Ex situ* synchrotron XRD of cycled electrodes of the pristine MnO<sub>2</sub> nanoparticles (Figure 3) shows that after the first cycle both akhtenskite and ramsdellite phases are largely converted to a new lithiated phase with broad features between 18-22, at 35 and at 45 degrees (Figure 3 and S5, supplemental information). This phase's reflection positions are in good agreement with LiMn<sub>2</sub>O<sub>4</sub> (LMO), which is considered to be a promising cathode for high power density LIBs [36-38]. The *in situ* formation of LMO results in a high initial capacity of 278 mAh g<sup>-1</sup>. With cycling the characteristic peak between 18-22 degrees broadens (Figure 3) and decreases in intensity suggesting loss of crystallinity and amorphization of this phase consistent with decay in the electrochemical performance. It has been reported that the electrochemical performance of LiMn<sub>2</sub>O<sub>4</sub> significantly depends on its crystallinity and crystallite size and it suffers from Mn dissolution into the electrolyte in the presence of acidic species by disproportionation, resulting in performance degradation [36-38]. There is no significant change in the diffraction patterns of

the cathode material in the charged state and discharge state of each cycle (Figure 3 and S5, supplemental information), indicating the persistence of the  $\text{LiMn}_2\text{O}_4$  structure with Li vacancies after de-lithation .

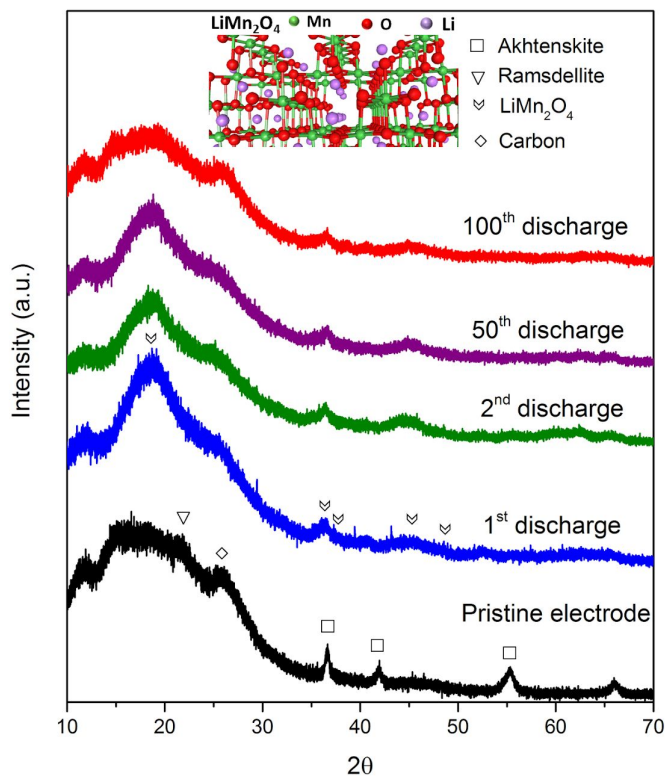


Figure 3. Synchrotron XRD patterns of unycled and cycled **pristine  $\text{MnO}_2$  nanoparticles** in the 1<sup>st</sup>, 2<sup>nd</sup>, 50<sup>th</sup> and 100<sup>th</sup> discharged states.

Table 2. Discharge capacities in the 1<sup>st</sup> and 100<sup>th</sup> cycles and capacity retention after 25<sup>th</sup> cycle of pristine and annealed  $\text{MnO}_2$  nanoparticles.

Sample	1 <sup>st</sup> discharge capacity ( $\text{mAh g}^{-1}$ )	100 <sup>th</sup> discharge capacity ( $\text{mAh g}^{-1}$ )	Capacity retention over 75 cycles (%)

P	278 ± 14	94 ± 13	55
A270	237 ± 27	116 ± 13	74
A320	247 ± 29	94 ± 24	59
A400	283 ± 2	126 ± 3	77

These results show the significance of thermal treatment as a tool to improve the redox reversibility and capacity retention of MnO<sub>2</sub> as LIB cathodes. Specifically, it can reduce the variability of phase composition between different batches without change in particle morphology and facilitate the conversion of less ordered structures such as akhtenskite, ramsdellite and gamma phase to more ordered pyrolusite polymorph with 1 × 1 channels, which has shown the best cycling performance as LIB cathode amongst other polymorphs. Additionally, we have demonstrated electrochemical *in situ* formation of a highly active LiMn<sub>2</sub>O<sub>4</sub>-like phase - bypassing the complexity of chemical synthesis of this compound, which resulted in high initial capacity. The performance fading of the MnO<sub>2</sub> nanoparticles is most likely due to the amorphization of the newly formed phase upon lithiation (Figure 3) and probably Mn dissolution due to the deep discharge [17].

### **Mechanical processing of the samples**

Since the crystal size, conductivity and crystallinity have been reported to play an important role in electrochemical performance of electroactive materials, specifically LiMn<sub>2</sub>O<sub>4</sub> [36-41], mechanical processing (high energy ball-milling) of the MnO<sub>2</sub> nanoparticles with graphite was investigated. Unlike thermal treatment, mechanical processing of the nanoparticles in a high energy ball-mill has a significant impact on the nanomaterial's morphology and crystallinity as a function of treatment time. As seen in Figure 4, at 20 min processing time (sample B20) most of the MnO<sub>2</sub> nanoplatelets maintain their morphology and are well dispersed within graphite

particles. Continuous ball-milling for longer times (40 min and 60 min) results in indistinct morphology of both MnO<sub>2</sub> and graphite (Figure 4c-d).

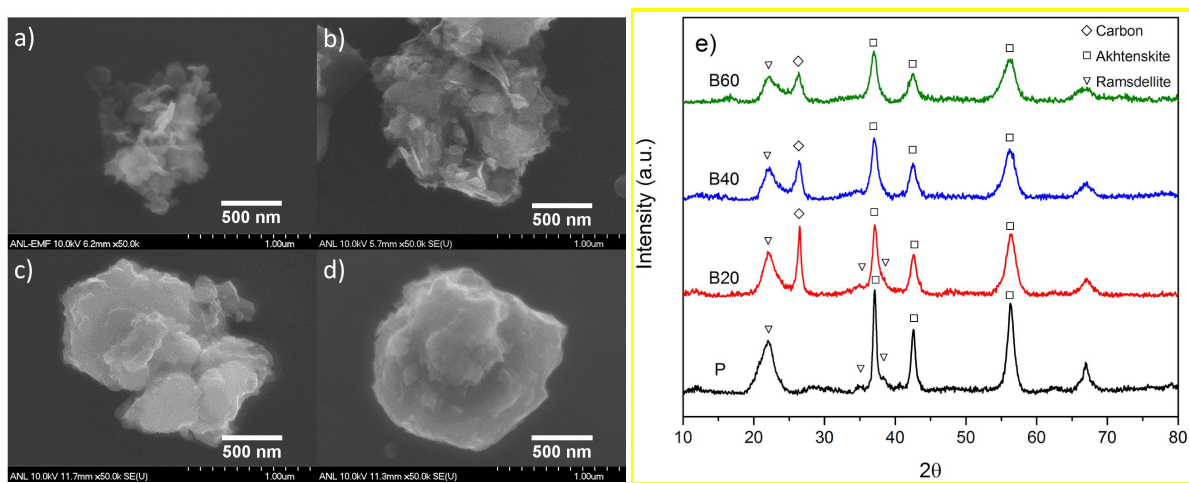


Figure 4. SEM images of a) pristine MnO<sub>2</sub>, b) B20, c) B40, d) B60 nanocomposites and XRD patterns of pristine and ball-milled MnO<sub>2</sub> nanoparticles.

The XRD patterns confirmed amorphization of both MnO<sub>2</sub> and graphite with increased processing times (Figure 4e). Nanoparticles ball-milled for 20 min (B20) are slightly amorphized, showing broader peaks with less intensity than pristine sample (Figure 4e). Rietveld refinement of the patterns shows smaller crystallite sizes (Table 3). A slight decrease in the ratio between ramsdellite and akhtenskite phase fraction ( $R/\epsilon$ ) is observed in the B20 sample. As the ball-milling time increases, the crystallite sizes of both MnO<sub>2</sub> and graphite decreases, as well as the  $R/\epsilon$  ratio. Even after 60 min of mechanical processing considerable amounts of crystalline ramsdellite and akhtenskite phases remain in the samples. The akhtenskite polymorph appears to be more physically stable at longer ball-milling times indicated by a decreasing trend in the  $R/\epsilon$  ratio from Rietveld refinement (Table 3).

*Ex situ* XANES spectra of the ball-milled samples (Figure 5a) show an increasing shift of the Mn K-edge to lower energies with ball-milling time, indicating reduction in average Mn oxidation state and is most likely related to the oxidation of the graphite during the ball-mill processing and elevated temperatures in the vessel.

Table 3. Polymorph composition, crystallite size and the ratio of ramsdellite to akhtenskite weight fractions (R/ε) from Rietveld refinement for pristine and ball-milled MnO<sub>2</sub> nanoparticles.

Sample	Ramsdellite		Akhtenskite		Graphite		R/ε
	wt%	crystallite size (nm)	wt%	crystallite size (nm)	wt%	crystallite size (nm)	
P	37 ± 1	3 × 3	63 ± 1	17 × 10	-	-	0.59
B20	30 ± 1	3 × 2	54 ± 1	12 × 6	16 ± 1	14 × 14	0.56
B40	28 ± 1	3 × 1	58 ± 1	7 × 5	14 ± 1	5 × 7	0.48
B60	27 ± 1	3 × 1	55 ± 1	7 × 4	18 ± 1	6 × 5	0.49

Cyclic voltammograms of the ball-milled samples (Figure 5b) show that current density in the first cycle decreases as the ball-milling time increases. Sample B60 showed the least redox activity amongst the samples. The results suggest the significance of sample crystallinity of MnO<sub>2</sub> nanoparticles and the conductive graphite additive in redox activity of the material.

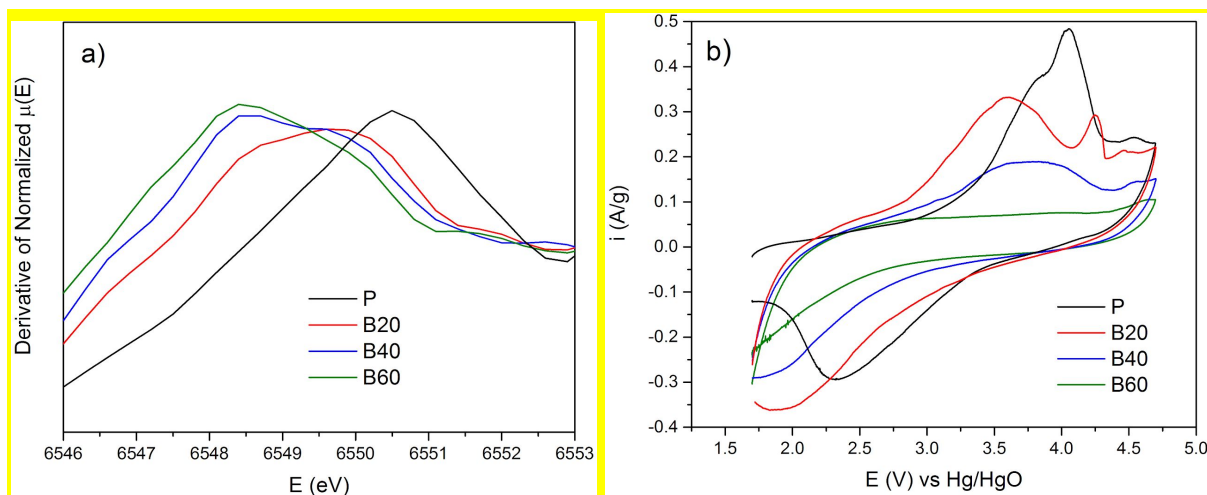


Figure 5. a) The derivatives of the XANES regions for pristine and ball-milled  $\text{MnO}_2$  nanoparticles from the *ex situ* XAS spectra at Mn K-edge and b) cyclic voltammograms of the pristine and ball-milled samples at 1<sup>st</sup> cycle and at  $0.5 \text{ mVs}^{-1}$ .

Galvanostatic cycling of electrodes showed better electrochemical performance of the B20 sample with initial capacity of  $319 \pm 8 \text{ mAh g}^{-1}$ , which gradually decreased upon cycling, but remained consistently higher than that of the pristine material. Ball-milling for longer times (B40 and B60 samples) resulted in a more rapid performance degradation (Figure 6a). By the 100<sup>th</sup> cycle, the capacity of sample B20 faded (Figure 6a) to a close but slightly higher value than the capacity of the pristine material (Table 4). Thus ball-mill processing for 20 min results in a composite with a slight crystallite size reduction, minimal amorphization, and a lower  $R/\epsilon$  ratio, which improves the capacity (Figure 4e and Table 3). However, significant capacity fading is observed in long term cycling.

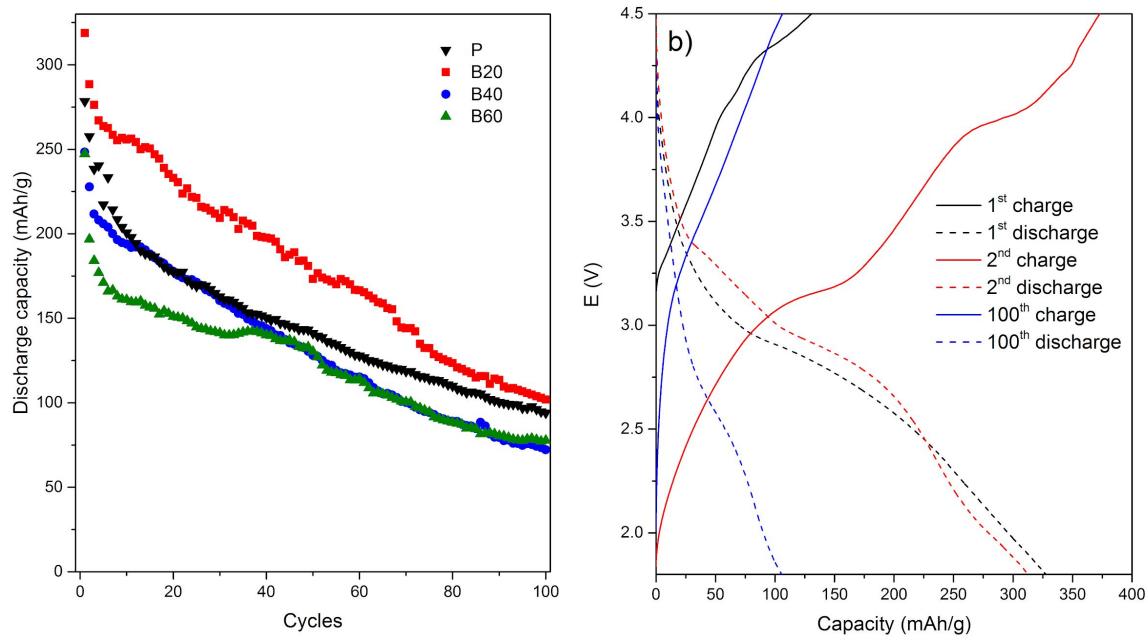


Figure 6. a) Galvanostatic cycling of the pristine and ball-milled MnO<sub>2</sub> nanoparticles and b) Galvanostatic charge/discharge curves of B20 sample.

Table 4. 1<sup>st</sup> and 100<sup>th</sup> discharge capacities and capacity retention from the 25<sup>th</sup> to the 100<sup>th</sup> cycle for pristine and ball-milled MnO<sub>2</sub> nanoparticles.

sample	1 <sup>st</sup> discharge capacity (mAh g <sup>-1</sup> )	100 <sup>th</sup> discharge capacity (mAh g <sup>-1</sup> )	Capacity retention over 75 cycles (%)
P	278 ± 14	94 ± 12	55
B20	319 ± 8	102 ± 6	46
B40	248 ± 23	72 ± 14	42
B60	247 ± 29	77 ± 7	54

Similar to the pristine sample, oxidation of  $\text{Mn}^{3+}$  to  $\text{Mn}^{4+}$  is observed in the first charge of B20 sample (Figure S4, supplemental information). Charge/discharge curves of B20 sample (Figure 6b) look very similar to those of the pristine sample with the exception of better defined plateaus on the second charge, which is likely due to facilitated  $\text{Li}^+$  removal and accessing the sites, which were not accessible in the pristine sample, resulting from smaller crystal size (Table 3) and higher conductivity from the graphite in the composite. The latter suggests similar lithiation mechanism in both P and B20 samples through *in situ* formation of electrochemically active  $\text{LiMn}_2\text{O}_4$ .

*In situ* XAS data (Figure 7a) correspond to P and B20 samples with first discharge capacities of 206  $\text{mAh g}^{-1}$  and 230  $\text{mAh g}^{-1}$  respectively (Figure 7b). The results show that while both P and B20 samples are in nearly the same oxidation state at OCV and in the charged state (Figure 7b, S6 and Table S1, Supplemental information), B20 is less reduced in the first discharge compared to the pristine sample (Figure 7a). *Ex situ* spectra after 100 cycles (Figure 7c) show a smaller energy shift in discharged states compared to the first cycle (Figure 7a) in agreement with the lower observed capacity. B20 extracted electrode, which delivered higher 100<sup>th</sup> discharge capacity than the pristine electrode (95  $\text{mAh g}^{-1}$  vs 78  $\text{mAh g}^{-1}$ ), showed more change in oxidation state than pristine in 100<sup>th</sup> discharge (Figure 7c), in agreement with the galvanostatic cycling results (Figure 6a).

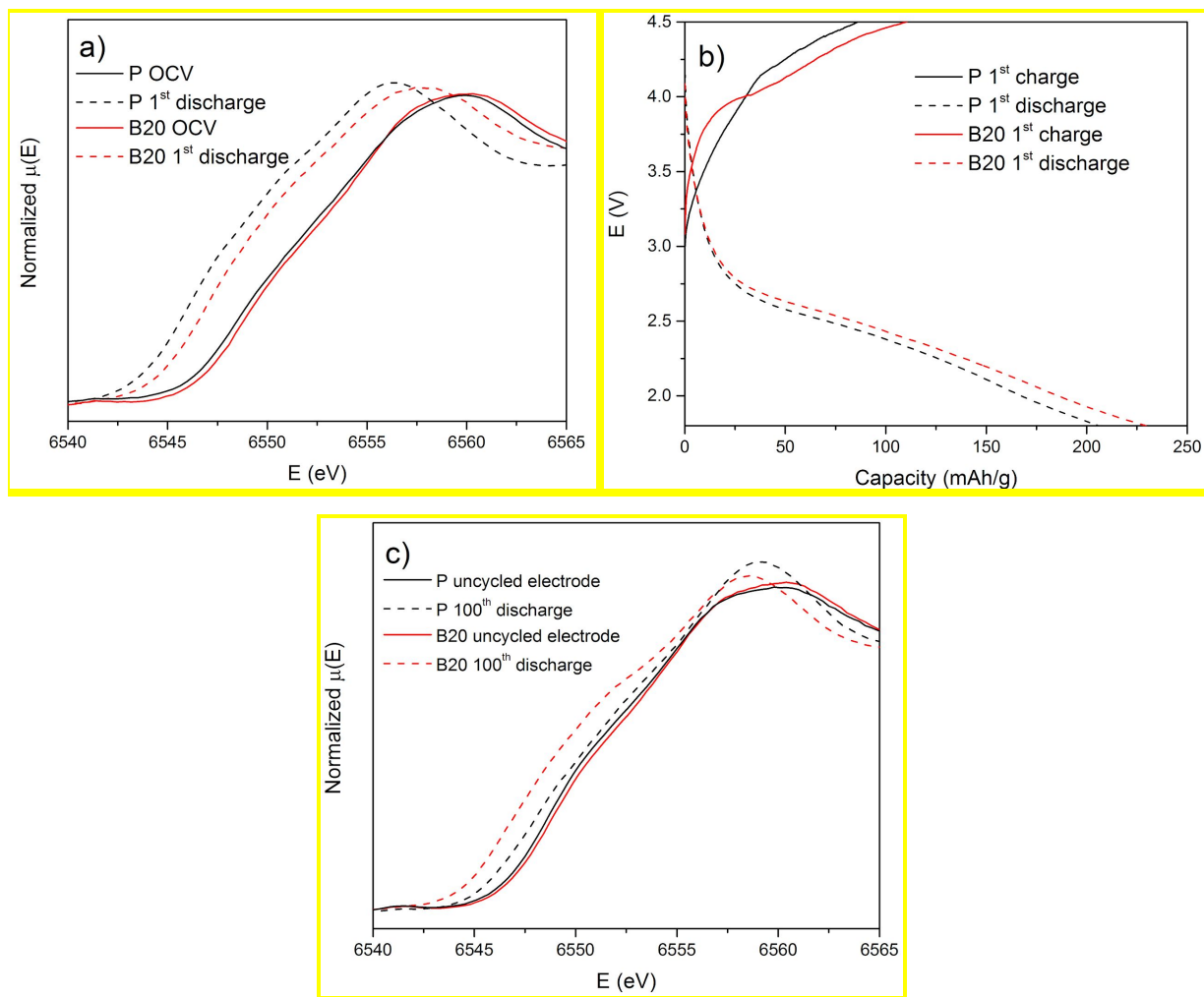


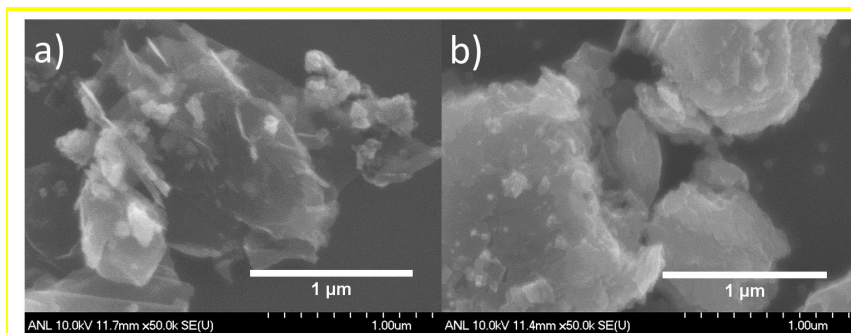
Figure 7. a) *In situ* XANES regions, b) galvanostatic charge/discharge curves (C/10) and c) *ex situ* XANES regions of XAS spectra at the Mn K-edge, for P and B20 *in situ* pouch cells.

The higher initial capacity in some ball-milled samples suggests the importance of the crystallinity, crystal size, accessibility due to better contact with the conductive material and local environment for electrochemical performance, while rapid capacity fading is likely related to  $Mn^{2+}$  dissolution and capacity fading mechanism of pristine material which most likely includes amorphization of  $LiMn_2O_4$ -like phase by cycling.

### Combination of thermal and mechanical processing techniques

Improved capacity retention was observed in A270 and A400 samples highlighting the significant effect of both water removal and concentration of pyrolusite domains on the reversible intercalation of Li ions. On the other hand, ball-milling for moderate times results in enhanced initial capacity (B20), most likely due to improved conductivity introduced by well-mixed graphite and smaller crystallite size. Therefore, a possible synergistic effects of thermal and mechanical processing and the treatment order were investigated by annealing pristine MnO<sub>2</sub> nanoparticles from the same batch at 270 °C, followed by ball-milling for 20 min (AB sample) and ball-milling the pristine nanoparticles, followed by annealing at 270 °C (BA sample).

A lower degree of amorphization for the AB sample was observed compared to the BA sample, showing more defined MnO<sub>2</sub> platelets in this sample in SEM images (Figure 8a and b), suggesting that the order of processing affects the morphology and level of amorphization.



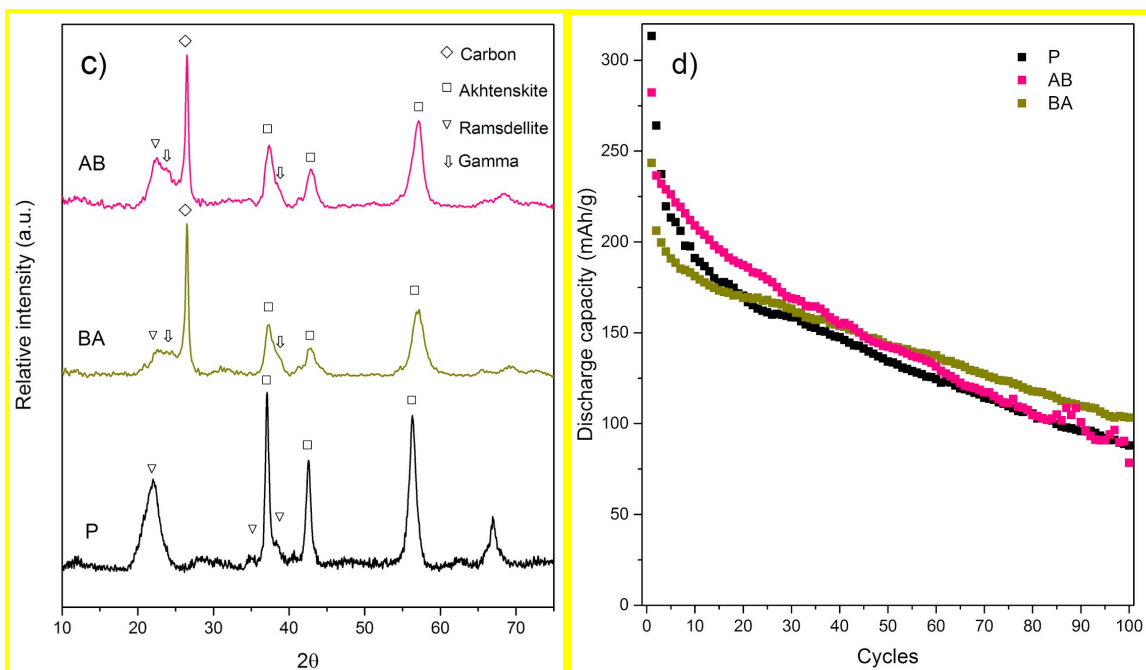


Figure 8. SEM images of a) annealed-ball-milled (AB) and b) ball-milled-annealed (BA)  $\text{MnO}_2$  nanoparticles and c) XRD patterns and d) Galvanostatic cycling for pristine, AB and BA nanoparticles at C/10 charge rate.

The XRD patterns also showed more amorphization for  $\text{MnO}_2$  nanoparticles in the BA sample compared to the AB sample probably due to the facilitated structural water removal from the stressed structure resulting from ball-milling (Table 5 and Figure 8c). As the Rietveld refinement results in Table 5 show, in the AB sample the ramsdellite and akhtenskite weight fractions are significantly decreased to  $9 \pm 1$  wt% and  $38 \pm 1$  wt%, respectively and  $19 \pm 1$  wt% gamma phase has formed. However, in BA, while ramsdellite is almost completely converted to gamma phase, which has a slightly bigger crystal size than gamma in AB (Table 5), the akhtenskite fraction is only decreased to  $48 \pm 1$  wt%. The  $\text{MnO}_2$  nanoparticles in both BA and AB samples were amorphized more than the ball-milled samples showing that the combination of the techniques has a more destructive effect upon the crystalline phases than ball-milling alone (Figure 8c and S7, supplemental information).

AB sample showed slightly higher discharge capacity than pristine nanoparticles in the initial cycles (Figure 8d), most likely due to smaller crystallite sizes and improved conductivity due to

ball-milling with graphite. BA sample showed slightly better capacity retention in long cycling, which could be attributed to almost complete elimination of the ramsdellite phase and higher concentration of the  $1 \times 1$  channels.

Although there is still room for processing optimization as far as combination of techniques goes to better control crystallinity, morphology and phase composition of  $\text{MnO}_2$  cathode, there appears to be no significant synergistic effect in the presented combination of treatments.

Table 5. Rietveld refinement results and capacity retention after 25<sup>th</sup> cycle of XRD patterns of the pristine, annealed-ball-milled (AB) and ball-milled-annealed (BA)  $\text{MnO}_2$  nanoparticles.

Sample	Ramsdellite		Akhtenskite		Gamma		GNP		Capacity retention over 75 cycles (%)
	wt%	crystallite size (nm)	wt%	crystallite size (nm)	wt%	crystallite size (nm)	wt%	crystallite size (nm)	
P	$37 \pm 1$	$3 \times 3$	$63 \pm 1$	$17 \times 10$	-	-	-	-	55
AB	$9 \pm 1$	$6 \times 3$	$38 \pm 1$	$9 \times 7$	$19 \pm 1$	$10 \times 3$	$34 \pm 1$	$1 \times 18$	43
BA	$1 \pm 1$	$16 \times 52$	$48 \pm 1$	$7 \times 6$	$28 \pm 1$	$10 \times 2$	$23 \pm 1$	$2 \times 23$	61

## Conclusions

In this study the effects of thermal and mechanical processing on performance of  $\text{MnO}_2$  nanoparticles as a cathode for Li-ion batteries were investigated. As-synthesized nanoparticles composed of ramsdellite and akhtenskite polymorphs (37 : 63 wt%) showed  $278 \text{ mAh g}^{-1}$  initial discharge capacity, but rapid capacity fading. Thermal treatment at  $400 \text{ }^\circ\text{C}$  resulted in conversion of initial phases to pyrolusite without change in particle morphology and improved cycle stability with discharge capacity of  $126 \pm 3 \text{ mAhg}^{-1}$  after 100 cycles. Synchrotron *ex situ* XRD investigation of lithiation and capacity fading mechanism suggests conversion of the original

phases to a lithiated  $\text{LiMn}_2\text{O}_4$ -like phase after the first cycle. This newly formed phase with smaller crystallite sizes, participates in reversible lithiation/de-lithiation during charge and discharge cycles. Capacity fading correlates with loss of crystallinity of this electrochemically formed phase during cycling. Ball-milling of the nanoparticles with graphite for 20 min resulted in smaller crystallite sizes, higher crystalline akhtenskite to ramsdellite ratio, and significantly higher  $319 \pm 8 \text{ mAh g}^{-1}$  initial capacity likely due to better conductivity within the sample. Capacity fading, however, is a remaining issue for this composite cathode. Longer ball-milling times resulted in more amorphous samples, lower capacity and faster capacity fading. The combination of thermal and mechanical processes and the order of treatments was also investigated. The results suggest that the order of the two treatments has a significant effect on the level of amorphization and morphology of the nanocomposites. The combination of the treatments results in higher amorphization for the same processing time than ball-milling alone. Despite differences in the sample morphology that was achieved, no significant synergistic effect between the processing methods can be reported.

## **Acknowledgements**

This research used resources of the Advanced Photon Source (APS) and Center for Nanoscale Materials (CNM) and Electron Microscopy Center (EMC), U.S. Department of Energy (DOE) Office of Science User Facilities operated for the DOE Office of Science by Argonne National Laboratory under Contract No. DE-AC02-06CH11357. APS beamline 11-BM was used for synchrotron X-ray powder diffraction and beamlines 10-BM and 10-ID for synchrotron X-ray absorption spectroscopy. MRCAT operations are supported by the Department of Energy and the MRCAT member institutions.

## **References**

- [1] Robertson, A.D. and Bruce, P.G., 2003. Mechanism of electrochemical activity in  $\text{Li}_2\text{MnO}_3$ . *Chemistry of Materials*, 15(10), pp.1984-1992.
- [2] Dose, W.M., Sharma, N. and Donne, S.W., 2014. Discharge mechanism of the heat treated electrolytic manganese dioxide cathode in a primary  $\text{Li}/\text{MnO}_2$  battery: An in-situ and ex-situ synchrotron X-ray diffraction study. *Journal of power sources*, 258, pp.155-163.
- [3] Ingale, N.D., Gallaway, J.W., Nyce, M., Couzis, A. and Banerjee, S., 2015. Rechargeability and economic aspects of alkaline zinc–manganese dioxide cells for electrical storage and load leveling. *Journal of Power Sources*, 276, pp.7-18.
- [4] Simon, D.E., Morton, R.W. and Gislason, J.J., 2004. A close look at electrolytic manganese dioxide (EMD) and the  $\gamma\text{-MnO}_2$  &  $\epsilon\text{-MnO}_2$  phases using Rietveld modeling. *Adv X-ray Anal*, 47, pp.267-280.
- [5] De Wolff, P.M., 1959. Interpretation of some  $\gamma\text{-MnO}_2$  diffraction patterns. *Acta Crystallographica*, 12(4), pp.341-345.
- [6] Ding, Y.S., Shen, X.F., Gomez, S., Luo, H., Aindow, M. and Suib, S.L., 2006. Hydrothermal growth of manganese dioxide into three-dimensional hierarchical nanoarchitectures. *Advanced Functional Materials*, 16(4), pp.549-555.
- [7] Lv, D., Huang, X., Yue, H. and Yang, Y., 2009. Sodium-Ion-Assisted Hydrothermal Synthesis of  $\gamma\text{-MnO}_2$  and Its Electrochemical Performance. *Journal of The Electrochemical Society*, 156(11), pp.A911-A916.
- [8] Rus, E.D., Moon, G.D., Bai, J., Steingart, D.A. and Erdonmez, C.K., 2016. Electrochemical behavior of electrolytic manganese dioxide in aqueous KOH and LiOH solutions: a comparative study. *Journal of The Electrochemical Society*, 163(3), pp.A356-A363.

- [9] Wolfenstine, J., Foster, D., Behl, W. and Gilman, S., 1998. Gas evolution and self-discharge in Li/MnO<sub>2</sub> primary batteries (No. ARL-TR-1805). ARMY RESEARCH LAB ADELPHI MD SENSORS AND ELECTRON DEVICES DIRECTORATE.
- [10] Ruetschi, P., 1984. Cation-Vacancy Model for MnO<sub>2</sub>. Journal of the Electrochemical Society, 131(12), pp.2737-2744.
- [11] Sarciaux, S., La Salle, A.L.G., Verbaere, A., Piffard, Y. and Guyomard, D., 1999.  $\gamma$ -MnO<sub>2</sub> for Li batteries: Part I.  $\gamma$ -MnO<sub>2</sub>: Relationships between synthesis conditions, material characteristics and performances in lithium batteries. Journal of power sources, 81, pp.656-660.
- [12] Jung, W.I., Sakamoto, K., Pitteloud, C., Sonoyama, N., Yamada, A. and Kanno, R., 2007. Chemically oxidized manganese dioxides for lithium secondary batteries. Journal of Power Sources, 174(2), pp.1137-1141.
- [13] Ohzuku, T., Kitagawa, M. and Hirai, T., 1990. Electrochemistry of Manganese Dioxide in Lithium Nonaqueous Cell II. X-Ray Diffractational and Electrochemical Characterization on Deep Discharge Products of Electrolytic Manganese Dioxide. Journal of The Electrochemical Society, 137(1), pp.40-46.
- [14] Tan, H., Wang, S. and Lei, X., 2015. New Insights for the Cyclic Performance of Li/MnO<sub>2</sub> Batteries Using a Simple Electrochemical Process. Journal of The Electrochemical Society, 162(3), pp.A448-A452.
- [15] Minakshi, M., Singh, P. and Mitchell, D.R., 2007. Manganese dioxide cathode in the presence of TiS<sub>2</sub> as additive on an aqueous lithium secondary cell. Journal of The Electrochemical Society, 154(2), pp.A109-A113.
- [16] Bowden, W., Grey, C.P., Hackney, S., Wang, F., Paik, Y., Iltchev, N. and Sirotna, R., 2006. Lithiation of ramsdellite–pyrolusite MnO<sub>2</sub>; NMR, XRD, TEM and electrochemical investigation of the discharge mechanism. Journal of power sources, 153(2), pp.265-273.

- [17] Thackeray, M.M., Rossouw, M.H., Gummow, R.J., Liles, D.C., Pearce, K., De Kock, A., David, W.I.F. and Hull, S., 1993. Ramsdellite-MnO<sub>2</sub> for lithium batteries: The ramsdellite to spinel transformation. *Electrochimica acta*, 38(9), pp.1259-1267.
- [18] Moazzen, E., Timofeeva, E.V., Kaduk, J.A. and Segre, C.U., 2019. Effect of sub-nanoparticle architecture on cycling performance of MnO<sub>2</sub> battery cathodes through thermal tuning of polymorph composition. *Crystal Growth & Design*, 19(3), pp.1584-1591.
- [19] Dose, W.M. and Donne, S.W., 2013. Heat treated electrolytic manganese dioxide for primary Li/MnO<sub>2</sub> batteries: Effect of manganese dioxide properties on electrochemical performance. *Electrochimica Acta*, 105, pp.305-313.
- [20] Shao-Horn, Y., Hackney, S.A. and Cornilsen, B.C., 1997. Structural Characterization of Heat-treated Electrolytic Manganese Dioxide and Topotactic Transformation of Discharge Products in the Li-MnO<sub>2</sub> Cells. *Journal of the Electrochemical Society*, 144(9), pp.3147-3153.
- [21] Moazzen, E., Timofeeva, E.V. and Segre, C.U., 2017. Controlled synthesis of MnO<sub>2</sub> nanoparticles for aqueous battery cathodes: polymorphism–capacity correlation. *Journal of materials science*, 52(13), pp.8107-8118.
- [22] Azmi, B.M., Ishihara, T., Nishiguchi, H. and Takita, Y., 2005. LiVOPO<sub>4</sub> as a new cathode materials for Li-ion rechargeable battery. *Journal of power sources*, 146(1-2), pp.525-528.
- [23] Kam, K.C., Gustafsson, T. and Thomas, J.O., 2011. Synthesis and electrochemical properties of nanostructured Li<sub>2</sub>FeSiO<sub>4</sub>/C cathode material for Li-ion batteries. *Solid State Ionics*, 192(1), pp.356-359.
- [24] Lee, J.H., Yoon, C.S., Hwang, J.Y., Kim, S.J., Maglia, F., Lamp, P., Myung, S.T. and Sun, Y.K., 2016. High-energy-density lithium-ion battery using a carbon-nanotube–Si composite anode and a compositionally graded Li [Ni<sub>0.85</sub>Co<sub>0.05</sub>Mn<sub>0.10</sub>]O<sub>2</sub> cathode. *Energy & Environmental Science*, 9(6), pp.2152-2158.

- [25] Ding, Y., Li, Z.F., Timofeeva, E.V. and Segre, C.U., 2018. In Situ EXAFS-Derived Mechanism of Highly Reversible Tin Phosphide/Graphite Composite Anode for Li-Ion Batteries. *Advanced Energy Materials*, 8(9), p.1702134.
- [26] Zhou, Y.K., He, B.L., Zhang, F.B. and Li, H.L., 2004. Hydrous manganese oxide/carbon nanotube composite electrodes for electrochemical capacitors. *Journal of Solid State Electrochemistry*, 8(7), pp.482-487.
- [27] Rietveld, H., 1969. A profile refinement method for nuclear and magnetic structures. *Journal of applied Crystallography*, 2(2), pp.65-71.
- [28] Larson, A. C.; Von Dreele, R. B. General Structure Analysis System (GSAS); Los Alamos National Laboratory Report LAUR 86-748; The Regents of the University of California: Oakland, CA, 2000.
- [29] Toby, B.H., 2001. EXPGUI, a graphical user interface for GSAS. *Journal of applied crystallography*, 34(2), pp.210-213.
- [30] FIZ Karlsruhe. ICSD. <https://icsd.fiz-karlsruhe.de/search/index.xhtml> (accessed Oct 21, 2016).
- [31] Kropf, A.J., Katsoudas, J., Chattopadhyay, S., Shibata, T., Lang, E.A., Zyryanov, V.N., Ravel, B., McIvor, K., Kemner, K.M., Scheckel, K.G. and Bare, S.R., 2010, June. The new MRCAT (Sector 10) bending magnet beamline at the advanced photon source. In *AIP Conference Proceedings* (Vol. 1234, No. 1, pp. 299-302). AIP.
- [32] Segre, C.U., Leyarovska, N.E., Chapman, L.D., Lavender, W.M., Plag, P.W., King, A.S., Kropf, A.J., Bunker, B.A., Kemner, K.M., Dutta, P. and Duran, R.S., 2000, June. The MRCAT insertion device beamline at the Advanced Photon Source. In *AIP Conference Proceedings* (Vol. 521, No. 1, pp. 419-422). AIP.

- [33] Ravel, B. and Newville, M.A.T.H.E.N.A., 2005. ATHENA, ARTEMIS, HEPHAESTUS: data analysis for X-ray absorption spectroscopy using IFEFFIT. *Journal of synchrotron radiation*, 12(4), pp.537-541.
- [34] Newville, M., 2001. IFEFFIT: interactive XAFS analysis and FEFF fitting. *Journal of synchrotron radiation*, 8(2), pp.322-324.
- [35] W.S. Rasband, ImageJ Software, vol. 2012, National Institutes of Health, Bethesda, MD, USA, 1997.
- [36] Ding, Y.L., Xie, J., Cao, G.S., Zhu, T.J., Yu, H.M. and Zhao, X.B., 2011. Single-Crystalline  $\text{LiMn}_2\text{O}_4$  Nanotubes Synthesized Via Template-Engaged Reaction as Cathodes for High-Power Lithium Ion Batteries. *Advanced Functional Materials*, 21(2), pp.348-355.
- [37] Lee, H.W., Muralidharan, P., Ruffo, R., Mari, C.M., Cui, Y. and Kim, D.K., 2010. Ultrathin spinel  $\text{LiMn}_2\text{O}_4$  nanowires as high power cathode materials for Li-ion batteries. *Nano letters*, 10(10), pp.3852-3856.
- [38] Kim, D.K., Muralidharan, P., Lee, H.W., Ruffo, R., Yang, Y., Chan, C.K., Peng, H., Huggins, R.A. and Cui, Y., 2008. Spinel  $\text{LiMn}_2\text{O}_4$  nanorods as lithium ion battery cathodes. *Nano letters*, 8(11), pp.3948-3952.
- [39] Liu, X., Chen, C., Zhao, Y. and Jia, B., 2013. A review on the synthesis of manganese oxide nanomaterials and their applications on lithium-ion batteries. *Journal of Nanomaterials*, 2013.
- [40] Moazzen, E., Timofeeva, E.V. and Segre, C.U., 2017. Role of crystal lattice templating and galvanic coupling in enhanced reversible capacity of  $\text{Ni}(\text{OH})_2/\text{Co}(\text{OH})_2$  core/shell battery cathode. *Electrochimica Acta*, 258, pp.684-693.
- [41] Guo, Y.G., Hu, J.S. and Wan, L.J., 2008. Nanostructured materials for electrochemical energy conversion and storage devices. *Advanced Materials*, 20(15), pp.2878-2887.